Available online at www.sciencedirect.com
ScienceDirect
Trans. Nonferrous Met. Soc. China 33(2023) 3250−3265
Transactions of Nonferrous Metals Society of China
www.tnmsc.cn

Microstructure, mechanical properties, and corrosion behavior of 6061 Al alloy prepared by cold spray-friction stir processing composite additive manufacturing

Zhi-hao LIU[1,2#], Peng HAN[1#], Wen WANG[1], Xiao-hu GUAN[1], Zhi WANG[1], Yuan FANG[1], Ke QIAO[1], Dong-ming YE[1], Jun CAI[1], Ying-chun XIE[2], Kuai-she WANG[1]

1. National and Local Joint Engineering Research Center for Functional Materials Processing, School of Metallurgical Engineering, Xi'an University of Architecture and Technology, Xi'an 710055, China;
2. Guangdong Provincial Key Laboratory of Modern Surface Engineering Technology, National Engineering Laboratory of Modern Materials Surface Engineering Technology, Institute of New Materials, Guangdong Academy of Sciences, Guangzhou 510651, China

Received 30 March 2022; accepted 13 July 2022

Abstract: Bulk 6061 aluminum (Al) alloy was prepared by cold spray-friction stir processing composite additive manufacturing (CFAM). The microstructures of the cold sprayed (CS) and CFAM samples were characterized by OM, SEM and EBSD, and their mechanical properties and corrosion behavior were investigated by microhardness, tensile and corrosion tests. The results show that, compared with the CS sample, the microstructure of the CFAM sample is densified and homogenized. The grains are small and equiaxed with an average grain size of 3.1 μm. The microhardness, ultimate tensile strength, and elongation of the CFAM sample are increased by 22%, 171%, and 683%, respectively. The corrosion current density of CFAM sample is 95.1%−97.8% lower than that of CS sample, and the corrosion mechanism is changed from pitting corrosion of CS sample to intergranular corrosion.

Key words: cold spray-friction stir processing composite additive manufacturing (CFAM); 6061 Al alloy; microstructure; mechanical properties; corrosion mechanism

1 Introduction

6061 aluminum (Al) alloy is widely used in the automotive industry due to its high strength and excellent corrosion resistance, and it is mainly prepared using casting and smelting methods, in which large amounts of waste is generated [1,2]. Additive manufacturing is a near-net-shape technology that enables the customization of complex parts and significantly improves material utilization [3]. Traditional technologies that use laser/electron beams as heat sources include selective laser melting (SLM), laser engineering net shaping (LENS), laser metal deposition (LMD), and electron-beam melting (EBM) [4−7]. The materials prepared by these traditional methods usually have high porosity and coarse structural defects [8]. Although the static strength is equivalent to that of the forgings, the plasticity and corrosion resistance are worse [9,10]. Furthermore, it is difficult to achieve the additive manufacturing of high-reflectivity Al alloys by traditional laser additive manufacturing [11].

Cold spraying (CS) is also called cold gas dynamic spray or kinetic spray. During CS, particles

# Zhi-hao LIU and Peng HAN contributed equally to this work
Corresponding author: Wen WANG, Tel: +86-13720527194, E-mail: wangwen2025@126.com;
Ying-chun XIE, Tel: +86-18802034895, E-mail: yingchun0824@163.com
DOI: 10.1016/S1003-6326(23)66331-9

are accelerated by a low-temperature, high-pressure gas and impact the substrate, causing severe plastic deformation for the particles. In this way, the particles are deposited layer-by-layer. CS can avoid solidification structure defects and coarse grains in the traditional additive manufacturing processes. Therefore, the technique has already been used to prepare metal materials [12]. CS, as a solid-state additive technology, is not limited by the size of the raw materials and does not require a protective gas [13,14]. However, the materials prepared by CS still have some defects, such as high porosity, poor organizational uniformity, and weak interfacial bonding strength between particles, resulting in low plasticity and poor corrosion resistance [15]. For example, QIU et al [16] used CS to prepare a bulk A380 Al alloy with a porosity of 1.3%, a micropore diameter of approximately 5 μm, and the ultimate tensile strength (UTS) of 230 MPa, while the elongation (EL) of only 3%. In addition, HUTASOIT et al [17] showed that the higher porosity of CS 6061 Al alloy deteriorated its pitting resistance, and the maximum pit depth reached 396 μm. Similarly, GUO et al [18] showed that a bulk Al prepared by CS had many micropores, which acted as diffusion channels for the corrosion medium and deteriorated the corrosion resistance.

Friction stir processing (FSP) is a severe plastic deformation technology developed from friction stir welding. It involves inserting a stirring tool with a specific stirring pin and shoulder into the workpiece, which is then subjected to the dual action of friction and stirring by the high-speed rotating stirring tool. This process causes severe plastic deformation and dynamic recrystallization and refines, densifies, and homogenizes the material [19]. Recently, FSP has been used to modify the CS coatings. For example, KHODABAKHSHI et al [20] used FSP to modify the CS 7075 Al alloy coating, its structure was significantly densified, homogenized, and refined, and its microhardness increased by three times. HUANG et al [21] modified the CS Cu−Zn coating with FSP. The results showed that the UTS of the modified Cu−Zn coating increased from 87 to 258 MPa, and the EL increased from 0.17% to 0.81%. Similarly, HUANG et al [22] used FSP to modify the SiC_p/Al5056 composite coating prepared by CS. The SiC particles in the composite coating were refined from 12.2 to 4.4 μm, showed a uniform distribution, and the composite microhardness increased from HV 95 to HV 185. A similar conclusion was obtained by HODDER et al [23]. The above studies show that FSP can significantly refine, densify, and homogenize CS materials.

Combining the technical advantages of CS and FSP, in this research a new solid additive manufacturing technology called cold spray-friction stir additive manufacturing (CFAM) was proposed. The main technical principles are as follows: the first step is to use CS to pre-prepare an additive layer of a certain thickness on the surface of the selected substrate. In the second step, multi-pass FSP is performed on the prepared additive layer to refine, homogenize, and densify the microstructure. In the third step, the first two steps are repeated. CS and FSP are used alternately to obtain a complete target bulk material layer-by-layer. CFAM can fundamentally solve the problems caused by single CS additive manufacturing, such as high porosity, uneven structures, and weak bonding strength between particles. It provides an effective method to prepare light metal components with excellent comprehensive mechanical properties.

Our previous research showed that the bulk of pure Al prepared by CFAM was refined, homogenized, and densified. Compared with CS sample, CFAM significantly reduced the porosity of the CS material, and the UTS and EL were increased by 45% and 1336%, respectively [24]. However, there have been no reports on the preparation of bulk 6061 Al alloy by CFAM, and the microstructure evolution, mechanical properties, and corrosion behavior are unclear. Therefore, a bulk 6061 Al alloy was prepared by CFAM in this study. The microstructure, mechanical properties, and corrosion behavior of the CS and CFAM samples were investigated, and the corrosion mechanisms were discussed to demonstrate that CFAM technology can provide a novel ideal for the preparation of Al alloy.

2 Experimental

2.1 Materials

Commercial 6061 Al alloy powder (prepared by nitrogen atomization) was used as the raw material. The particle size distribution of the original powder was measured by a laser particle

size analyzer (KM1-JL−1156). The particle morphology is shown in Fig. 1(a), in which most particles had an irregular spherical shape. The surface of the particles was rough (Fig. 1(b)). The average particle size was 28.4 μm (Fig. 1(c)). The XRD pattern of the raw material showed that no second phases were detected in the 6061 Al powder (Fig. 1(d)). This was because the 6061 Al particles were prepared by gas atomization and the second phases were dissolved into the Al matrix.

2.2 CFAM procedure

Figure 2(a) shows the schematic diagram of the CFAM process. A 6061 Al alloy deposition layer was prepared on the surface of a pure Al substrate using CS equipment (LERMPS-UTBM). The accelerating gas was nitrogen, the gas pressure and temperature were 5.0 MPa and 500 °C, respectively, the powder feed rate was 8 rad/min, and the moving speed of the spray gun was 200 mm/s. Subsequently, as shown in Fig. 2(a), FSP

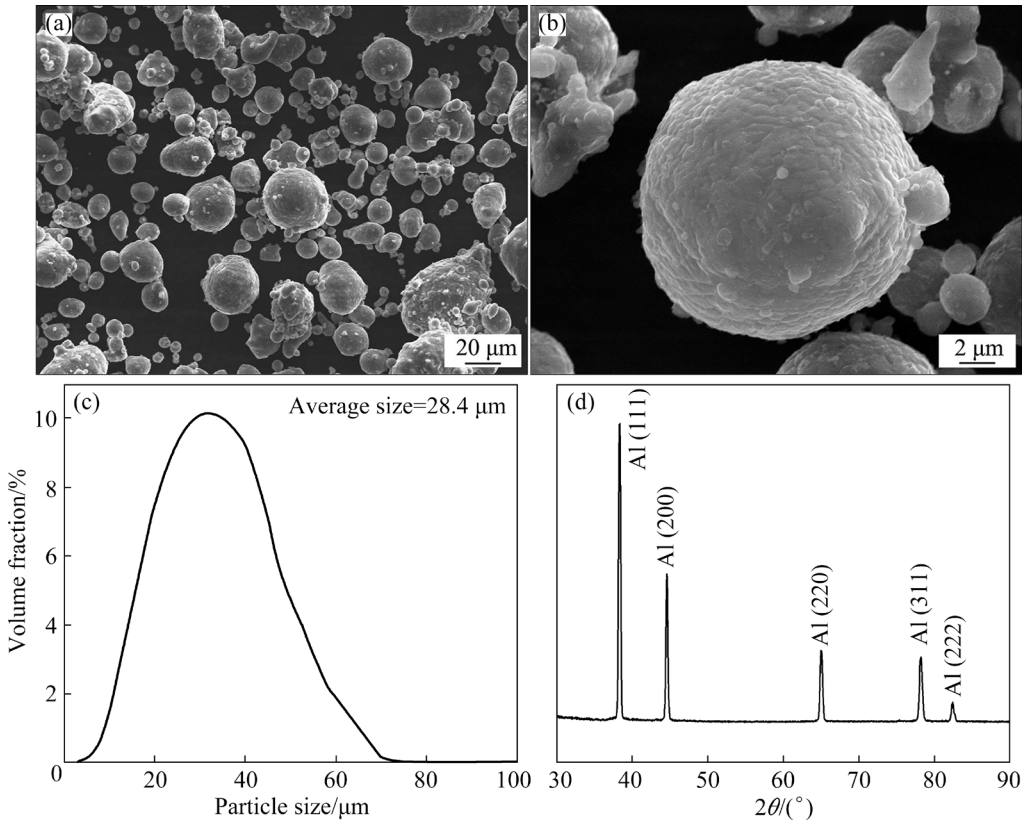

Fig. 1 Microstructure and size distribution of as-received 6061 Al powder: (a) SEM image; (b) Surface topography of one selected particle; (c) Size distribution; (d) XRD pattern

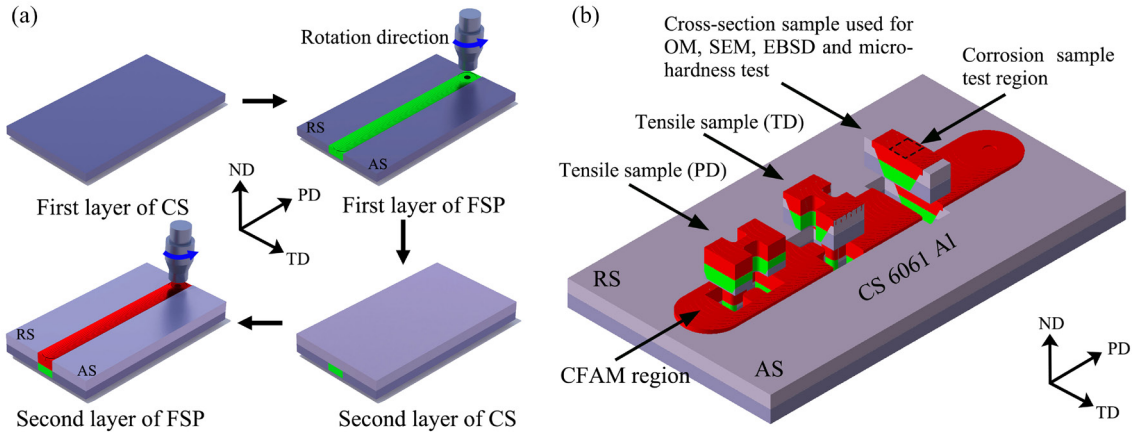

Fig. 2 Schematic illustration of CFAM (a) and sampling location (b) (TD, ND, and PD represent transversal, normal, and processing directions, respectively; AS and RS represent the advancing and retreating sides, respectively)

was performed on the surface of the CS deposition using FSP equipment (FSW-LM-AM16−2D). Then, the CS and FSP processes were repeated on the surface of the deposit using the same process parameters. To investigate the mechanism of CFAM, single-pass FSP was used in this work. The diameter of the shoulder was 18 mm, the diameter of the cylindrical stirring pin was 7 mm, and the length was 3.8 mm. The rotational speed of the stirring tool was 1200 r/min, the processing speed was 45 mm/min, the shoulder reduction was 0.2 mm, and the inclination angle was 2°.

2.3 Microstructure characterization

The phase structures of the CS and CFAM samples were tested by XRD (Bruker D8 ADVANCE-A25). In the XRD phase detection, a Cu K_α target, with a wavelength of 1.54 Å, a scanning step size of 0.02°, and an operating voltage and current of 40 kV and 40 mA, respectively, was used. CS and CFAM sample cross-sections were etched for 60 s using Keller's reagent (190 mL water, 5 mL nitric acid, 2 mL hydrofluoric acid, and 3 mL hydrochloric acid). An optical microscope (OM, OLYMPUS M3) and scanning electron microscope (SEM, Gemin SEM 300) equipped with electron backscatter diffraction (EBSD) were used to characterize the microstructures of CS and CFAM samples. The voltage was 20 kV, and the step size was 100 nm. The densities of CS and CFAM samples were tested and calculated by Archimedes' principle. The sampling position of the microstructure is shown in Fig. 2(b).

2.4 Mechanical properties test

The Vickers microhardness test was carried out on three sections of CFAM samples (ND−TD, TD−PD, and PD−ND planes) using an automatic microhardness tester (HXD−1000TM) at intervals of 0.5 mm, with a load of 100 g and pressure holding time of 10 s (Fig. 2(b)). An electro-hydraulic servo testing machine was used to measure the room-temperature tensile properties (Instron 8801). The initial strain rate was 1×10^{-3} s^{-1}, and three parallel samples were used. After the tensile tests, the fracture morphology of the tensile samples was observed by SEM.

2.5 Corrosion test

2.5.1 Immersion corrosion test

Immersion corrosion samples were cut from the center of the CS deposition layer and the CFAM region, respectively. The sample dimensions were 10 mm × 10 mm × 6 mm. Only the test surface was retained on the sample's surface, and the other surfaces were sealed with epoxy resin. The samples were immersed in 3.5 wt.% NaCl solution at room temperature for 24, 36, and 48 h, respectively. After soaking, the surface morphology of the samples was observed by SEM. The samples were weighed before and after soaking by using an analytical balance with an accuracy of 0.0001 g.

2.5.2 Electrochemical corrosion test

To observe the corrosion behavior of the samples during different corrosion processes, electrochemical experiments were carried out using an electrochemical workstation (P4000) by soaking samples in 3.5 wt.% NaCl solution for different time. Electrochemical tests were performed in three-electrode electrolyte cells. A sample worked as the working electrode, a platinum electrode as the auxiliary electrode, and a saturated calomel electrode (SCE) as the reference electrode. The medium was 3.5 wt.% NaCl solution. After 1 h immersion, polarization curves were measured in the voltage range from −1 to 2 V (vs the open-circuit potential (OCP)) at a scan rate of 1.5 mV/s. Electrochemical impedance spectroscopy (EIS) test was performed on the corresponding OCPs with a voltage amplitude of ±5 mV and a frequency from 100 kHz to 0.01 Hz.

3 Results and discussion

3.1 Microstructure

3.1.1 Microstructure of CS sample

Figure 3(a) shows the SEM image of the CS sample. Some micropores occur at the intersection of three adjacent particles. SHARMA et al [25] also observed triple junction voids when 6061 Al alloy was deposited with CS, which were formed due to the lack of local deformation during the deposition of some particles [26−28]. In addition, there is no obvious deformation inside the 6061 Al particles, the particle boundaries undergo severe plastic deformation, and the interface between the particles is clear. These results indicate that metallurgical bonding between the 6061 Al particles is weak. Even under adiabatic shear, the bonding mechanism is mainly the mechanical bonding, followed by the metallurgical bonding [29].

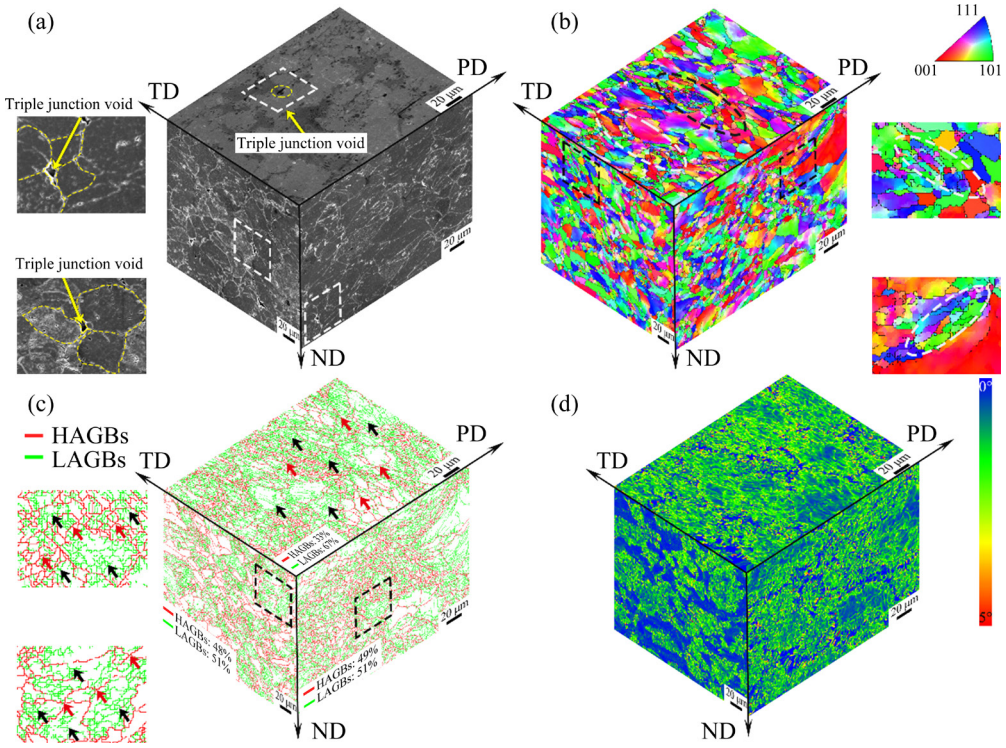

Fig. 3 SEM image (a), inverse polar figure (IPF) (b), grain boundaries (c), and KAM map (d) of CS sample

Figure 3(b) shows the inverse polar figure (IPF) of the CS sample. Along the PD, TD, and ND, the grain size distribution of CS samples is uneven, and there is no preferred orientation. Equiaxed and fine elongated grains (black ellipse) appear at the grain interface, and ultrafine grains (white ellipse) are also found. This is because the high-speed impact of the deposited grains during the CS process caused adiabatic shearing instability at the interface, triggering continuous dynamic recrystallization (CDRX) and geometric dynamic recrystallization (GDRX) at the Al particle interface [30−33]. In addition, the proportion of LAGBs in ND of the CS sample is as high as 67%, which are mainly distributed inside the Al grains (Fig. 3(c), black arrows). The HAGBs are mainly distributed at the Al grain interfaces (Fig. 3(c), red arrows). This indicates that more dislocation substructures are retained inside the particles, and the residual stress is comparatively large. The result is also reflected by the kernel average misorientation (KAM) map in Fig. 3(d). The above results demonstrate that the microstructure of the CS samples in different building directions is not uniform.

3.1.2 Microstructure of CFAM sample

Figure 4(a) shows the macroscopic cross-section of the CFAM region. It can be seen that the CFAM region has a “stacked basin shape” without defects such as pores or cracks. The CFAM region can be divided into the top, middle, and bottom regions due to different heat inputs and mechanical stirring in each region. The bottom region is subjected to the stirring action of the first FSP and the heat input of the second FSP, whereas the middle region is subjected to the double stirring action of FSP, and the top region is only subjected to the stirring action of the second FSP.

Figures 4(b−d) show the microstructures of the top, middle, and bottom regions of the CFAM sample, respectively. The grain size distributions of the top, middle and bottom regions are similar, all of which are fine and equiaxed grains with an average grain size of 2.7, 3.3, and 3.4 μm, respectively (Figs. 4(b_1−d_1)). The average grain size of the whole CFAM sample is 3.1 μm and has no preferred orientation. Compared with the CS sample, the CFAM sample has equiaxed grains due to the combined effect of the mechanical stirring of the stirring tool and frictional heat, which leads to recrystallization [22]. In addition, the proportion of HAGBs in the top, middle, and bottom regions are 64%, 72%, and 74%, respectively (Figs. 4(b_2−d_2)), and the average proportion of HAGBs is 70%. The grain boundaries of the CFAM samples consist of

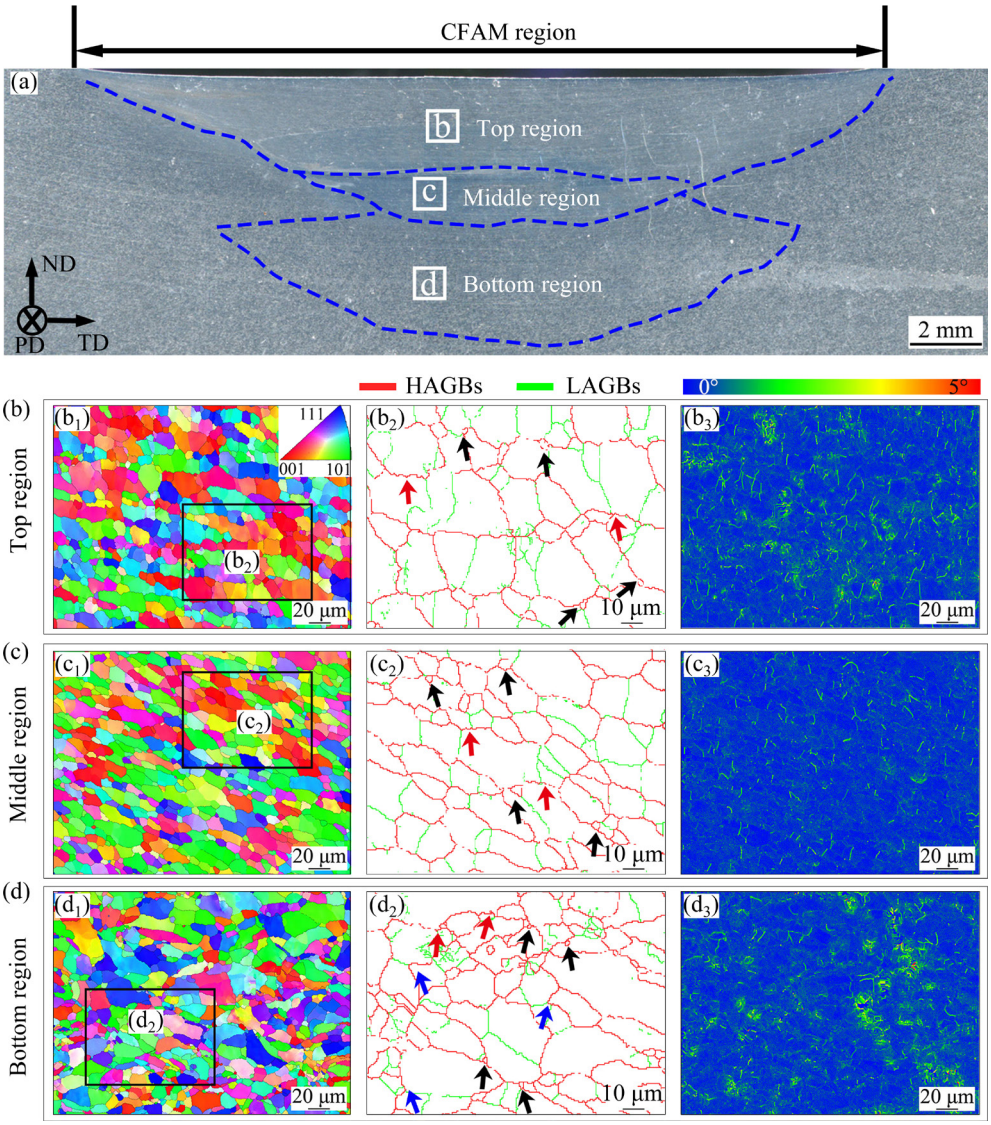

Fig. 4 Cross-sectional macrostructure of CFAM region (a), microstructure of top (b), middle (c), and bottom (d) regions: (b_1−d_1) IPF image; (b_2−d_2) grain boundaries; (b_3−d_3) KAM map

incomplete HAGBs and fine grains (black arrows), showing typical CDRX characteristics [34]. In addition, the appearance of jagged HAGBs indicates that GDRX occurs in the CFAM sample (Figs. 4(b_2−d_2), red arrows) [35]. WANG et al [36] also observed GDRX in Al alloys during FSW. The combined action of the heat input and the mechanical stirring of the pin in the bottom region provides a strong driving force for recrystallization, and the recrystallized grains are severely deformed. Many fine "chain-like" HAGBs occur at the grain boundaries, which are typically composed of fine equiaxed recrystallized grains and exhibit discontinuous dynamics (DDRX) characteristics (Fig. 4(d_2), blue arrows). It is generally believed that Al alloys are not prone to DDRX due to their high stacking fault energy [37], but the recrystallization mechanism is related to the initial state of the material. In this study, the initial state of the material at the bottom of the CFAM sample is recrystallized grains that undergo a single pass of FSP. The fine recrystallized grains are subjected to the combined action of heat input and stirring force to generate DDRX.

Compared with the CS sample, the dislocation density of the CFAM sample is significantly lower, and the KAM values are concentrated in the range of 0°−1° (the blue region of Figs. 4(b_3−d_3)). The dislocation density is the lowest in the middle region and the highest in the bottom region. Due to the double-stirring action of FSP in the middle region, the dynamic recrystallization occurs twice,

and the dislocation density decreases significantly. Under the effect of the second pass of FSP, some grains are coarsened in the bottom region. Meanwhile, the grains are deformed due to the downward force of the stirring pin during the second pass FSP, thus showing a slightly higher dislocation density.

To study the uniformity of the CFAM sample in different building directions, the microstructure in different directions is characterized in Fig. 5. The grain distributions of the CFAM sample along the PD, TD, and ND are uniform, fine and equiaxed, with an average grain size of 3.3, 3.2, and 2.8 μm, respectively. The average grain size of the whole CFAM sample is 3.1 μm, and there is no preferred orientation (Fig. 5(b)). Similar to the microstructural characteristics in the thickness direction of the CFAM samples, the three different directions of the CFAM samples show higher proportions of HAGBs (>70%) and lower levels of dislocation density (Figs. 5(c) and (d)). Compared with the CS sample, the interfaces between Al particles in the CFAM sample are eliminated, and the porosity decreases (Fig. 5(a)). The results obtained using Archimedes' principle show that the density of the CFAM sample is ~2.7 g/cm^3, which is 106% higher than that of the CS sample. The above studies show that the bulk 6061 Al alloy prepared by CFAM is dense, uniform, and non-isotropic.

3.1.3 XRD patterns

The XRD patterns of the CS and CFAM samples are shown in Fig. 6. In the figure, all samples exhibit a consistent intensity peak angle closest to the Al-FCC phase, which is identical compared to the feedstock powder (Fig. 1(d)). The intensity peaks of the precipitates, such as Mg_2Si phase, are not found in CS and CFAM samples. Generally, the low temperature and limited time during CS deposition would not lead to the precipitation of Mg_2Si phase. Furthermore, rapid dissolution of the second phase usually occurs during FSP [38]. Therefore, the effects of the second phase on the mechanical properties and corrosion behaviors of CS and CFAM samples are not discussed in this study.

3.2 Mechanical properties

3.2.1 Microhardness

Figure 7 shows the microhardness of the CFAM sample (the PD−ND plane is the section at the black dotted line). It can be seen that the average microhardness value of the CS region is about HV 45, while that of the CFAM region is about HV 55. Compared with the CS region, the microhardness of the CFAM region is increased by 22%. This is because CFAM eliminates the micropores, improves the bonding strength between particles, and significantly densifies and

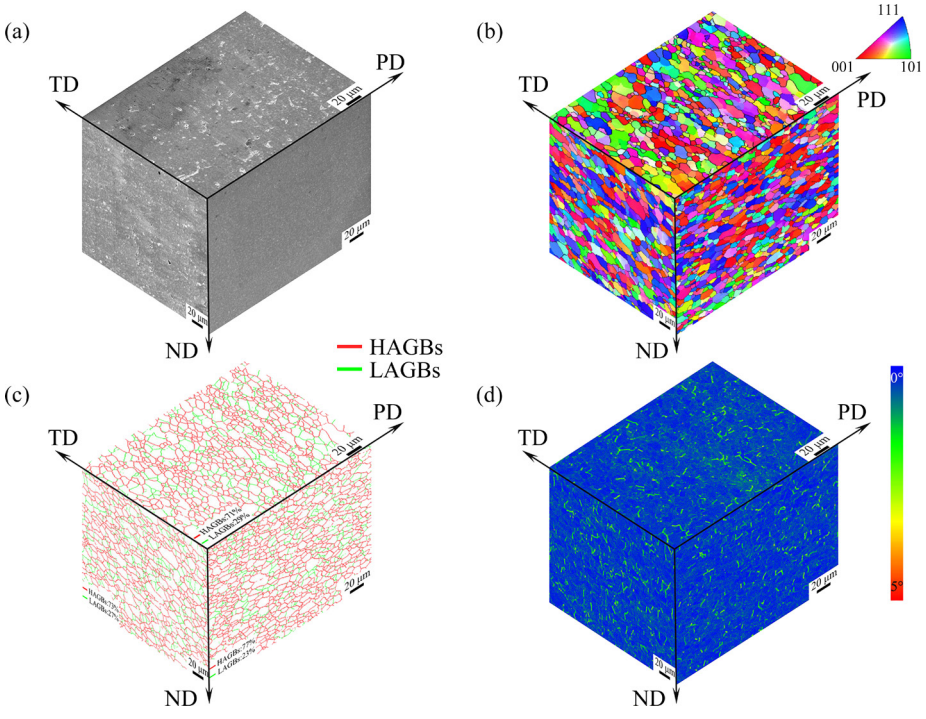

Fig. 5 SEM image (a), IPF image (b), grain boundaries (c), and KAM map (d) of CFAM sample

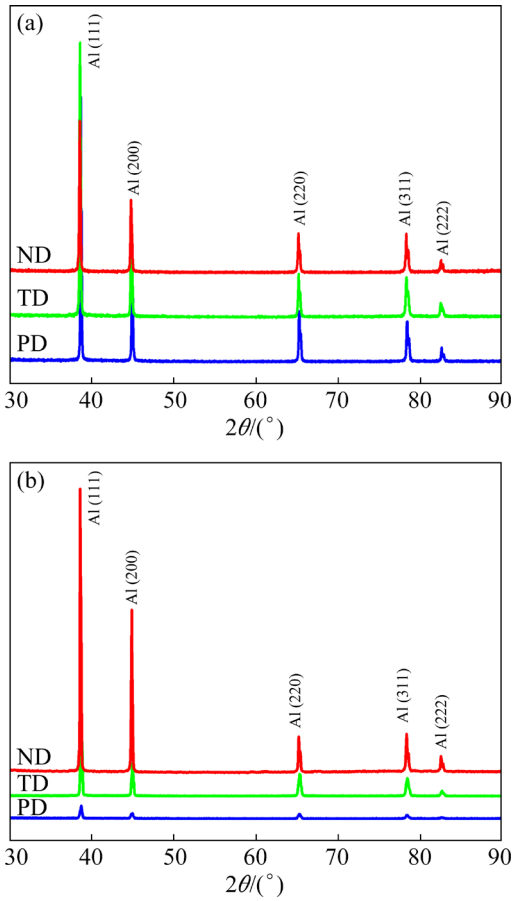

Fig. 6 XRD patterns of CS (a) and CFAM (b) samples

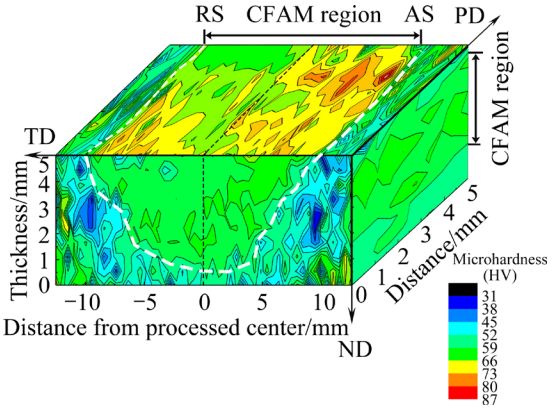

Fig. 7 Microhardness of CFAM sample

homogenizes the microstructure of the CS sample. In future work, the precipitation phase in the CFAM region should be controlled by heat treatment, thereby further improving the microhardness of the CFAM sample. It is worth noting that the microhardness value on the advancing side in the CFAM region is slightly higher than that on the retreating side, because the material on the advancing side is sheared more strongly than that on the retreating side by the stirring pin [39].

3.2.2 Tensile properties

Figure 8(a) shows the tensile properties along PD and TD of CS and CFAM samples. The UTS of the CS sample along the PD and TD is 74 and 64 MPa, respectively, and the EL is 6.7% and 7.1%, respectively. The tensile properties along the PD and TD are similar because both directions experienced adiabatic shear during the CS process, thus the bonding strength and bonding mechanism between particles are similar. By contrast, the UTS of the CFAM sample along the PD and TD is 166 and 174 MPa, respectively, and the EL is 45.4% and 55.6%, respectively. Similar to the CS sample, the UTS values along the PD and TD of CFAM sample are similar. Nevertheless, the EL along the TD is 22.5% higher than that along the PD. Compared with the CS sample, the UTS along the PD and TD of the CFAM sample is 124% and 171% higher, respectively, and the EL increases by 577% and 683%, respectively. The main reason for the high UTS and EL of the CFAM samples is the homogenization and densification of the microstructure. Furthermore, a high proportion of HAGBs enhances the strain hardening ability, which

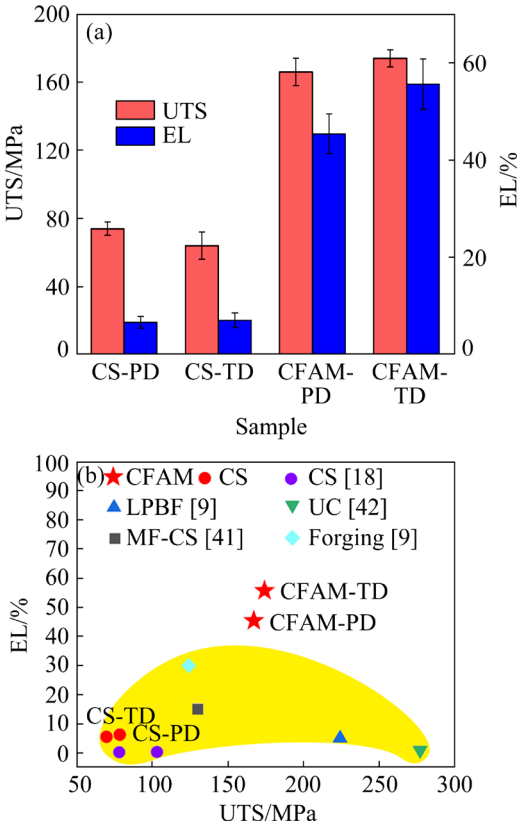

Fig. 8 Comparison of UTS and EL between CS and CFAM samples (a) and tensile property comparison of CFAM 6061 Al alloy obtained by different methods (b)

increases the strength and ductility of the CFAM sample [40].

Figure 8(b) compares the tensile properties of 6061 Al alloy prepared by CFAM, CS, in-situ forging-assisted cold spraying (MF-CS), laser powder bed fusion (LPBF), ultrasonic consolidation (UC) technology, and conventional forging [9,18,41,42]. The comprehensive strength and plastic properties of the CFAM samples in this study are better than those of the 6061 Al alloys prepared by CS, MF-CS, and forging. Furthermore, although the strength of the 6061 Al alloy prepared by CFAM is lower than that of the 6061 Al alloy prepared by LPBF and UC, the EL of the CFAM sample is greatly improved. This is because the CFAM sample has a uniform fine-grained structure and a high proportion of HAGBs [43].

Figure 9 shows the tensile fracture morphologies of CS and CFAM samples along the PD and TD. The fractures along the PD and TD in the CS sample show cracking along the Al particle interfaces. During the tensile process, the micropores induce stress concentration easily, leading to the rapid propagation of cracks, resulting in brittle fracture (Figs. 9(a) and (b)). In contrast to the CS sample, the fracture surface of the CFAM sample is distributed with many small dimples, showing the characteristics of ductile fracture. Notably, the dimples along the TD of the CFAM sample are finer and more uniform than those along the PD (Figs. 9(c) and (d)). It is well known that the larger the size of the dimples, the better the plasticity of the material [44,45]. However, the CFAM sample exhibits greater plasticity along the TD. This phenomenon can be attributed to two aspects. Firstly, the CFAM bulk is only subjected to the stirring action of a single pass of FSP. The defects in the CS deposit have not been completely eliminated. There are some tiny pores in the dimples of the CFAM sample along the PD (Fig. 9(c)). The pores reduce the actual area of force applied to the CFAM sample along the PD during the tensile process. This is the main reason for the lower strength and elongation of CFAM sample along the PD. Furthermore, the grain size in the CFAM sample along the TD is smaller than that along PD. The number of dimples in the fracture of the CFAM sample along the TD is more than that along PD. During the tensile process, the formation of dimples consumes energy and thus inhibits crack expansion, which leads to a large elongation in the CFAM sample along the TD [21].

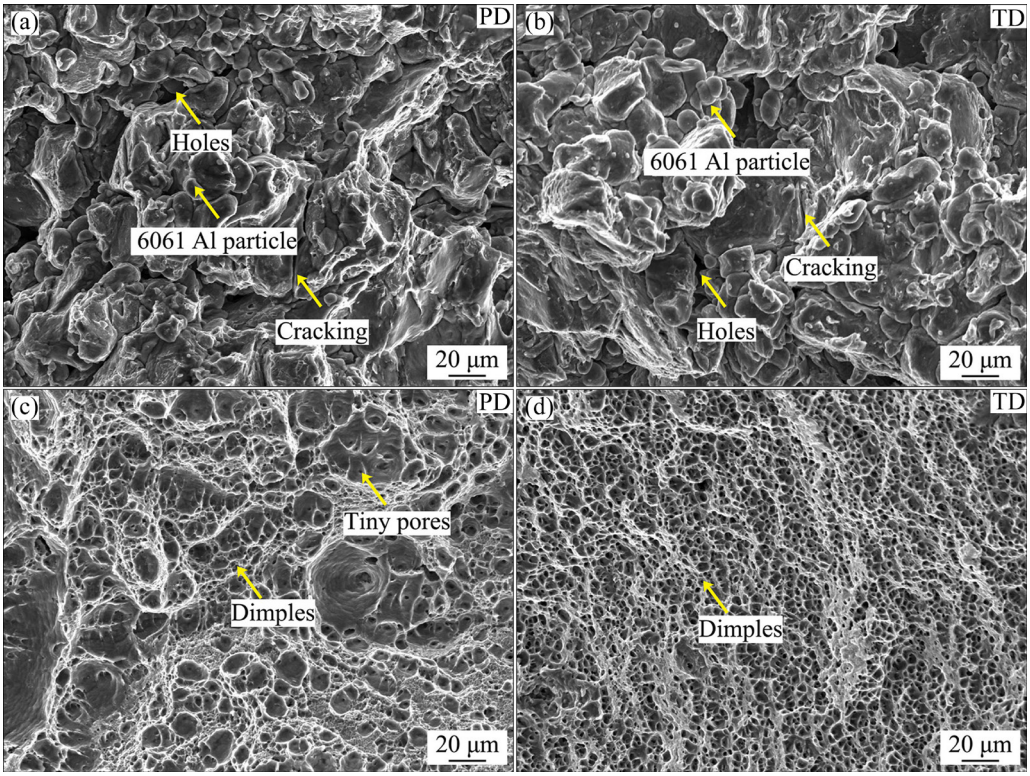

Fig. 9 SEM images showing fracture surface of tensile samples obtained by CS (a, b) and CFAM (c, d): (a, c) PD; (b, d) TD

3.3 Corrosion behaviors and mechanism

3.3.1 Immersion corrosion behavior

Figure 10 shows the surface morphologies of CS and CFAM samples immersed in NaCl solution for 24, 36, and 48 h, respectively. After 24 h of immersion, a large number of pits and large pores are distributed on the surface of the CS sample, and a small amount of oxide film appears inside the pores (Fig. 10(a)). As the immersion time increases to 36 h, pitting pits and holes on the surface of the sample increase and small numbers of discontinuous reticulated oxide films appear (Fig. 10(b)). When the immersion time is increased to 48 h, the discontinuous network oxide films are connected into sheets and completely covered on the surface of the sample (Fig. 10(c)). There is no obvious corrosion on the surface of the CFAM sample after immersion for 24 h (Fig. 10(d)). With the immersion time increasing to 36 h, a few corrosion pits appear on the surface of the sample (Fig. 10(e)). When the immersion time is further increased to 48 h, the grain boundaries on the surface of the sample become prominent, and small numbers of tiny corrosion pits appear within the grain (Fig. 10(f)). Compared with the CS samples, the CFAM samples show better corrosion resistance, which is mainly due to their uniform and dense microstructure. Therefore, the corrosion solution cannot easily penetrate the samples, thus inhibiting the corrosion process.

The mass of CS and CFAM samples gradually increases with increasing immersion time. After the CS sample is immersed in NaCl solution for 24 h, the corrosion of Cl^- leads to the increase of micropores on the sample surface and the mass loss (Fig. 10(g)). At the same time, the exposed matrix inside the pores is easily corroded, resulting in the formation of oxide film (Fig. 10(a)), which simultaneously causes the mass gain of the CS sample. After 36 h of immersion, a small amount of reticular oxide film appears on the surface of the sample, and the mass of the sample continues to increase. When the immersion time is increased to 48 h, the network oxide film completely covers the sample surface and the mass is increased by 5.1 mg compared with that before immersion. The CFAM samples show a smaller mass gain upon increasing the immersion time. When the CFAM sample is soaked for 48 h, the corrosion mass gain is only 0.5 mg, which is an order of magnitude lower than

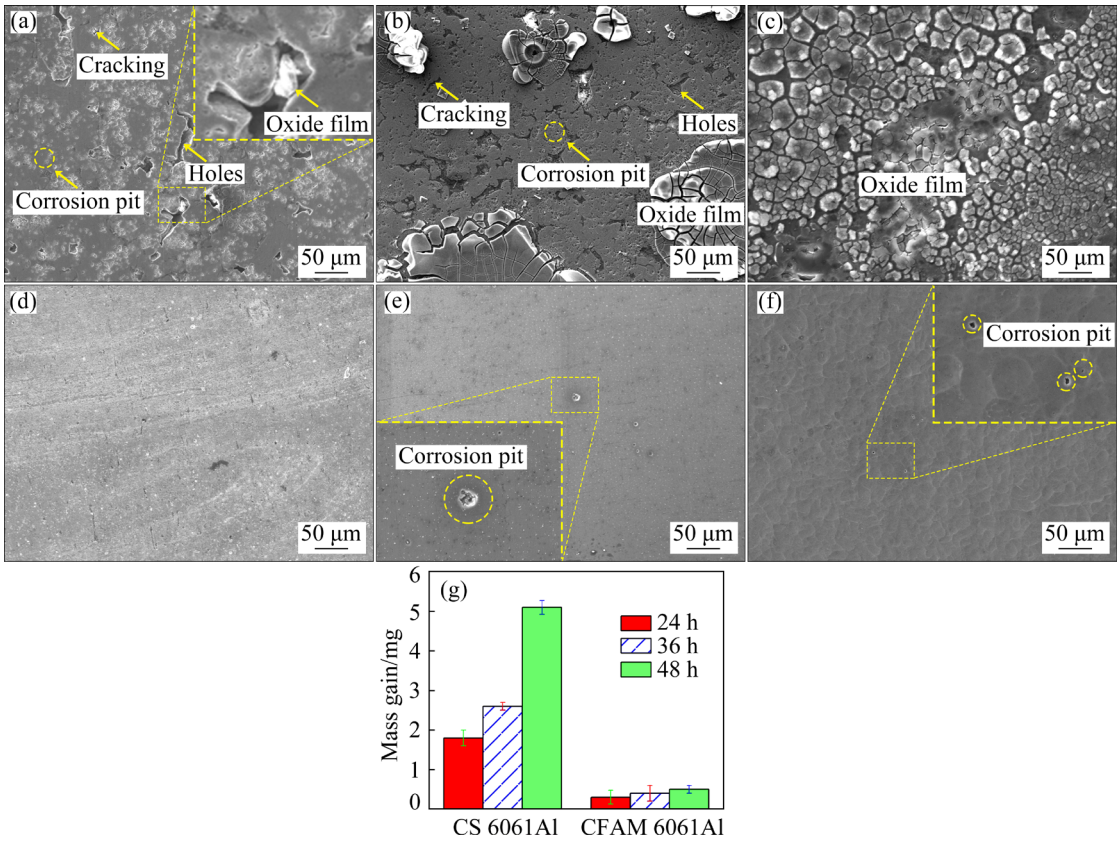

Fig. 10 Surface morphologies of CS (a−c) and CFAM (d−f) samples immersed in 3.5 wt.% NaCl solution for 24 h (a, d), 36 h (b, e), and 48 h (c, f), and mass gains of CS and CFAM samples (g)

that of the CS sample. Thus, the CFAM sample exhibits better corrosion resistance than the CS sample.

3.3.2 Electrochemical corrosion behavior

Figure 11 shows the open circuit potential (OCP), polarization curves, and electrochemical impedance spectroscopy (EIS) of CS and CFAM samples in NaCl solution. The corresponding corrosion potential (φ_{corr}) and corrosion current density (J_{corr}) are listed in Table 1. The OCP values of the CS samples are stable at about −0.7 V and show no significant differences with time (Fig. 11(a)). There are obvious passivation regions in the polarization curves (Fig. 11(b)), indicating that the corrosion oxide film has strong corrosion resistance and forms a protective effect on the samples [46]. In addition, the Nyquist plot of the CS sample has a single capacitive reactance arc (Fig. 11(c)), and its corrosion process has only one time constant. The corrosion process is a charge-transfer process that is kinetically controlled by electrochemical reactions [47].

For the CFAM sample, the OCP value is close to that of the CS sample (Fig. 11(d)), mainly because the surface components of the samples are similar and evenly distributed, which indicates that oxide films with similar properties were formed on the surfaces [48]. Compared with the CS sample, the CFAM sample exhibits a higher corrosion potential and wider passivation region (from −0.991 to −0.404 V) in the polarization curves (Fig. 11(e)), indicating that the CFAM sample has a low electrochemical activity. The CFAM sample maintains the stability of the passive state over a wide range of potentials [49]. In addition, compared with the CS sample immersed for the same time, the corrosion potential of the CFAM sample increases, and the corrosion current density is decreased by 95.1%−97.8% (Table 1), which indicates that the CFAM sample has better corrosion resistance. Different from the CS samples, the Nyquist plot characteristics of the CFAM samples show a capacitive arc in the high-frequency region and diffusion-controlled properties in the low-frequency region [50] (Fig. 11(f)). This is mainly due to the dense and uniform microstructure of CFAM samples, which inhibits the migration of corrosive ions. The low-frequency region exhibits diffusion-controlled properties.

To study the corrosion behavior of CS and CFAM samples, the Nyquist plots are fitted with an equivalent circuit, as shown in Figs. 12(a) and (b), respectively, and the relevant EIS fitting parameters are shown in Table 2, where R_s is the solution resistance; Q_f is the oxide film electrical double-layer capacitance; R_f is the oxide film resistance; Q_{dl} is the double-layer capacitance of the solution in contact with the substrate; R_{ct} is the charge transfer resistance of the dissolved substrate; C_f is the capacitor of the oxide film; W is the Warburg impedance, which is used to simulate diffusion-controlled processes at low frequencies; C_{cf} is the

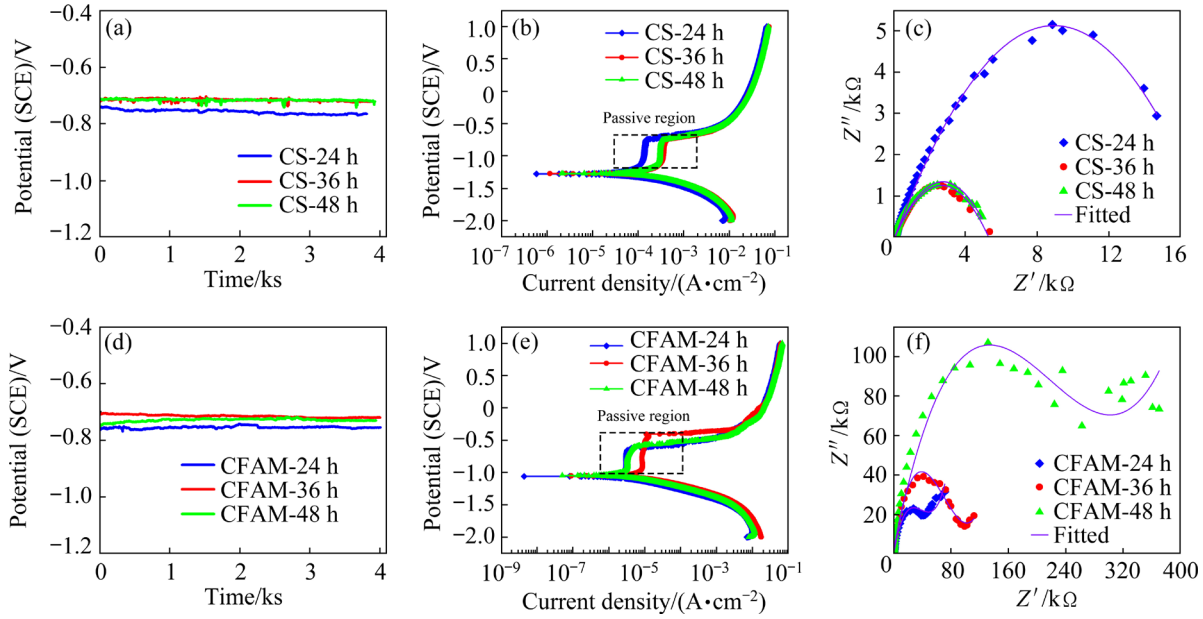

Fig. 11 OCPs (a, d), polarization curves (b, e) and EIS curves (c, f) of CS (a, b, c) and CFAM (d, e, f) samples in 3.5 wt.% NaCl solution

Table 1 Corrosion potential (φ_{corr}) and current density (J_{corr}) of CS and CFAM samples immersed in 3.5 wt.% NaCl solution for 24, 36, and 48 h, respectively

Sample	φ_{corr} (vs SCE)/V	J_{corr}/(μA·cm^{-2})
CS-24 h	−1.273±0.05	53.99±0.07
CS-36 h	−1.269±0.05	113.30±0.04
CS-48 h	−1.266±0.04	130.10±0.03
CFAM-24 h	−1.059±0.02	2.25±0.04
CFAM-36 h	−1.046±0.04	2.45±0.06
CFAM-48 h	−1.041±0.02	6.49±0.05

additive bulk capacitor element; R_{cf} is the additive bulk charge transfer resistor; n_f and n_{dl} are the migration indices of Q_f and Q_{dl}, respectively. Generally, the larger the values of R_f and R_{ct} are, the higher the corrosion resistance of a sample is [47]. For the CS samples, both R_f and R_{ct} decrease with increasing the immersion time, indicating that the charge transfer rate of matrix dissolution is accelerated during the corrosion process, and the corrosion resistance of the CS samples decreases. This is mainly due to the loose oxide film on the surface of the sample, and Cl^- penetrates the oxide film along its boundary to corrode the matrix.

Different from the CS samples, both R_f and R_{ct} in the CFAM samples increase with the increase of the immersion time, indicating that the charge transfer rate of the matrix dissolution is slow during corrosion. This is due to the formation of a dense oxide film during corrosion of the CFAM sample, which improves the corrosion resistance. Furthermore, the R_{ct} value of the CFAM sample increases significantly, indicating that its corrosion resistance is much higher than that of the CS sample.

3.3.3 Corrosion mechanism

KUMAR and RAO [51] pointed out that independent micropores can reduce the passivation stability of a sample and deteriorate its corrosion resistance. During the immersion corrosion process, due to the presence of pores in the CS sample, some of the fresh metal is in contact with the external corrosion medium, and large pores and tiny pits appear on the surface of the CS sample (Figs. 10(a−c)). The corrosion liquid invades the sample's interior along the large pores, and oxide film forms inside the micropores, showing typical pitting corrosion. At the same time, the surface of the CS sample is invaded by Cl^-, resulting in the formation of many small pits. Upon further corrosion, fine pits gradually enlarge and connect to form larger pores, resulting in the formation of

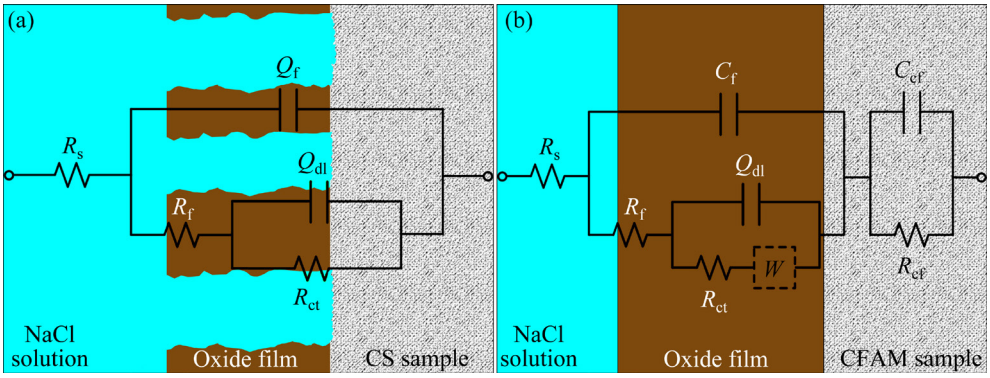

Fig. 12 Equivalent circuits for CS (a) and CFAM (b) samples

Table 2 Fitting results of EIS spectra for CS and CFAM samples

Sample	R_s/(Ω·cm^2)	Q_f (C_f)/(F·cm^{-2})	n_f	R_f/(Ω·cm^2)	Q_{dl}/(F·cm^{-2})	n_{dl}	R_{ct}/(Ω·cm^2)	W/(Ω·cm^2)	C_{cf}/(F·cm^{-2})	R_{cf}/(Ω·cm^2)
CS-24 h	100.30	1.016×10^{-4}	0.62	2160	1.220×10^{-6}	1.00	17570			
CS-36 h	92.43	4.356×10^{-5}	0.69	975	5.770×10^{-5}	0.72	3408			
CS-48 h	89.94	1.956×10^{-5}	0.76	874	6.658×10^{-6}	0.80	2494			
CFAM-24 h	104.10	6.252×10^{-7}		998	3.998×10^{-5}	0.80	56320	2.138×10^{-7}	3.264×10^{-6}	1.012×10^{5}
CFAM-36 h	110.20	1.374×10^{-6}		1030	2.122×10^{-6}	0.85	85980	1.657×10^{-6}	1.943×10^{-6}	1.125×10^{5}
CFAM-48 h	115.30	1.847×10^{-6}		1455	2.577×10^{-6}	0.85	245700	6.361×10^{-5}	4.833×10^{-5}	1.249×10^{5}

more oxide films, which cover the sample surface (Figs. 10(a−c)). The high density of the CFAM sample prevents the corrosion liquid from penetrating the sample interior along the micropores and inhibits the generation of corrosion products. Meanwhile, the surface of the CS sample is invaded by Cl^-, resulting in many tiny pits, which gradually expand and connect, thus forming larger pores and producing an oxide film that covers the sample's surface. The CFAM sample has a lower dislocation density, which weakens the micro-region stress corrosion effect and inhibits pitting corrosion [52], showing fewer pits and more uniform corrosion characteristics (Figs. 10(d−f)). In addition, the dislocation density at the grain boundary of the CFAM sample is higher than that in the grain, which is easily corroded. Therefore, intergranular corrosion eventually occurs (Fig. 10(f)).

During electrochemical corrosion, the oxide film formed on the surface of the CS sample after immersion corrosion falls off, making the micropores expose to the solution. Cl^- easily invades the sample interior via the micropores (Fig. 13(a_1)), which accelerates the corrosion process, showing a lower corrosion voltage and higher corrosion current density. The anodic and cathodic reactions of the CS samples during corrosion by the NaCl solution are Al matrix dissolution and dissolved oxygen reduction, respectively [53]:

$$Al=Al^{3+}+3e \quad (1)$$

$$O_2+2H_2O+4e=4OH^- \quad (2)$$

In addition, $Al(OH)_3$ precipitates during corrosion and then transforms into insoluble $Al_2O_3{\cdot}H_2O$ after encountering O_2 (Fig. 13(a_2)). As corrosion progresses, the corrosion pits get deeper, and corrosion products fill the pits and cracks, decreasing the transfer rate of Cl^- in the pits and cracks, thus increasing the contact time between Cl^- and corrosion products. The corrosion product $Al(OH)_3$ is invaded by Cl^- again, producing water-soluble $AlCl_3$, resulting in the dissolution of $Al(OH)_3$ and the deepening of corrosion pits (Fig. 13(a_3)). The specific reaction process is as follows:

$$Al^{3+}+3OH^-=Al(OH)_3 \quad (3)$$

$$2Al(OH)_3=Al_2O_3+3H_2O \quad (4)$$

$$Al(OH)_3+3Cl^-=AlCl_3+3OH^- \quad (5)$$

The anodic reaction of the CFAM sample in NaCl solution is the same as the cathodic reaction of the CS sample, except that during the electrochemical corrosion, the surface of the CFAM sample exhibits uniform and dense oxide films. At the beginning of corrosion, Cl^- replaces O^{2-} in the oxide film, thus decomposing the oxide film [54]. As a result, pitting corrosion is induced, and pits with different depths appear on the surface of the sample (Fig. 13(b_1)). Upon increasing the corrosion time, the oxide film gradually dissolves, the number of pits increases and the pits gradually expand under the erosion of Cl^- (Fig. 13(b_2)). The decomposition of the oxide film and the appearance of pitting pits allow Cl^- to intrude the Al matrix, resulting in the aggravated surface corrosion (Fig. 13(b_3)).

4 Conclusions

(1) The microstructure of CFAM samples in different building directions is uniform and dense, and there is no preferred orientation. Under the action of DDRX and CDRX, the grains are small and equiaxed with an average grain size of 3.1 μm, a low dislocation density and a high proportion of

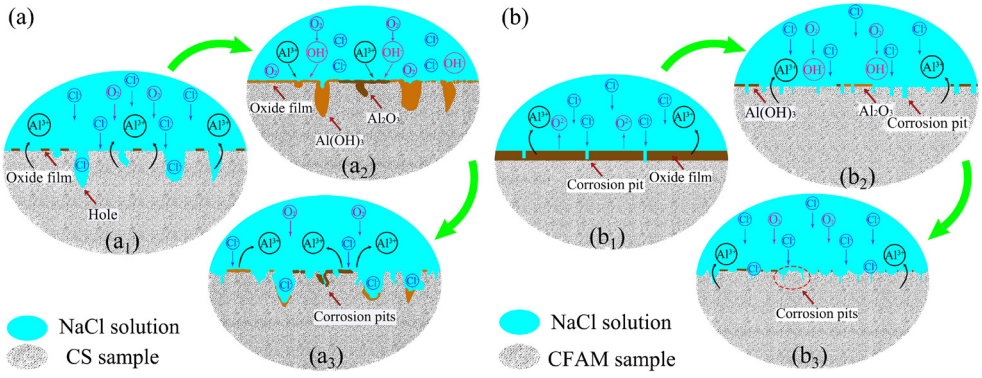

Fig. 13 Schematic diagrams of corrosion process for CS (a) and CFAM (b) samples

HAGBs (>70%). Compared with the CS sample, the density of the CFAM sample is 106% higher, reaching the theoretical density of the Al alloy.

(2) The average microhardness value of the CFAM sample reaches HV 55, which is 22% higher than that of the CS sample. The UTS along the PD and TD of the CFAM sample is similar, and the UTS and EL are increased by 171% and 683%, respectively, compared with the CS sample. The fractures of the CS samples show brittle fracture characteristics along the Al particles interfaces, while fractures of the CFAM samples are distributed with many small dimples, showing the characteristics of ductile fracture.

(3) During immersion corrosion, the primary corrosion mechanism of the CS sample is pitting corrosion. The CFAM sample shows excellent corrosion resistance, and the primary corrosion mechanism is pitting corrosion and intergranular corrosion. During electrochemical corrosion, the corrosion current density of the CFAM sample is 95.1%−97.8% lower than that of the CS sample, showing a higher corrosion voltage and lower corrosion current density.

Acknowledgments

The authors gratefully acknowledge the financial supports from the National Natural Science Foundation of China (Nos. 51974220, 52001078, 52104383, 52034005), the National Key Research and Development Program of China (No. 2021YFB3700902), the Shaanxi Provincial National Science Fund for Distinguished Young Scholars, China (No. 2022JC-24), and the Guangdong Basic and Applied Basic Research Foundation, China (No. 2019B1515120016).

References

[1] ZAIN-UL-ABDEIN M, NÉLIAS D. Effect of coherent and incoherent precipitates upon the stress and strain fields of 6xxx aluminium alloys: A numerical analysis [J]. International Journal of Mechanics and Materials in Design, 2016, 12(2): 255−271.

[2] TAN J H, WONG W L E, DALGARNO K W. An overview of powder granulometry on feedstock and part performance in the selective laser melting process [J]. Additive Manufacturing, 2017, 18: 228−255.

[3] BI Jiang, LIU Lei, WANG Chen-yang, CHEN Guang, JIA Xiang-dong, CHEN Xi, XIA Hong-bo, LI Xiao-peng, STAROSTENKOV M D, HAN Bing, DONG Guo-jiang. Microstructure, tensile properties and heat-resistant properties of selective laser melted AlMgScZr alloy under long-term aging treatment [J]. Materials Science and Engineering: A, 2022, 833: 142527.

[4] BI Jiang, CHEN Yan-bin, CHEN Xi, STAROSTENKOV M D, DONG Guo-jiang. Densification, microstructural features and tensile properties of selective laser melted AlMgSiScZr alloy from single track to block specimen [J]. Journal of Central South University, 2021, 28(4): 1129−1143.

[5] ZHANG Chi, LIU Yang, LU Jia-qi, XU li-ke, LIN Yao-jun, CHEN Ping-an, SHENG Qiang, CHEN Fei. Additive manufacturing and mechanical properties of martensite/ austenite functionally graded materials by laser engineered net shaping [J]. Journal of Materials Research and Technology, 2022, 17: 1570−1581.

[6] LIU Tian-yun, MIN Xiao-hua, ZHANG Shuang, WANG Cun-shan, DONG Chuang. Microstructures and mechanical properties of Ti−Al−V−Nb alloys with cluster formula manufactured by laser additive manufacturing [J]. Transactions of Nonferrous Metals Society of China, 2021, 31(10): 3012−3023.

[7] YANG Xin, WANG Wan-lin, MA Wen-jun, YANG Jun-gang, LIU Shi-feng, TANG Hui-ping. Corrosion and wear properties of micro-arc oxidation treated Ti_6Al_4V alloy prepared by selective electron beam melting [J]. Transactions of Nonferrous Metals Society of China, 2020, 30(8): 2132−2142.

[8] SINCLAIR-ADAMSON R, HARBIDGE M, MURRAY R. Sintering of cold spray additively manufactured aluminum 6061 [J]. Journal of Thermal Spray Technology, 2021, 30(6): 1493−1511.

[9] UDDIN S Z, MURR L E, TERRAZAS C A, MORTON P, ROBERSON D A, WICKER R B. Processing and characterization of crack-free aluminum 6061 using high-temperature heating in laser powder bed fusion additive manufacturing [J]. Additive Manufacturing, 2018, 22: 405−415.

[10] SZYMCZYK-ZIÓŁKOWSKA P, HOPPE V, GĄSIOREK J, RUSIN′SKA M, KEZSZYCKI D, SZCZEPAN′SKA Ł, DUDEK-WICHER R, DETYNA J. Corrosion resistance characteristics of a Ti−6Al−4V ELI alloy fabricated by electron beam melting after the applied post-process treatment methods [J]. Biocybernetics and Biomedical Engineering, 2021, 41(4): 1575−1588.

[11] LI Wen-ya, WU Dong, HU Kai-wei, HU Ya-xin, YANG Xia-wei, ZHANG Yong. A comparative study on the employment of heat treatment, electric pulse processing and friction stir processing to enhance mechanical properties of cold-spray-additive-manufactured copper [J]. Surface and Coatings Technology, 2021, 409: 126887.

[12] YANG Kang, LI Wen-ya, GUO Xue-ping, YANG Xia-wei, XU Ya-xin. Characterizations and anisotropy of cold-spraying additive-manufactured copper bulk [J]. Journal of Materials Science and Technology, 2018, 34(9): 1570−1579.

[13] ZOU Y. Cold spray additive manufacturing: microstructure evolution and bonding features [J]. Accounts of Materials Research, 2021, 2(11): 1071−1081.

[14] CHEN Chao-yue, XIE Ying-chun, LIU Long-tao, ZHAO Rui-xin, JIN Xiao-li, LI Shan-qing, HUANG Ren-zhong, WANG Jiang, LIAO Han-lin, REN Zhong-ming. Cold spray

additive manufacturing of Invar 36 alloy: Microstructure, thermal expansion and mechanical properties [J]. Journal of Materials Science and Technology, 2021, 72: 39−51.

[15] CAVALIERE P, SILVELLO A. Fatigue behaviour of cold sprayed metals and alloys: Critical review [J]. Surface Engineering, 2016, 32(9): 631−640.

[16] QIU Xiang, TARIQ N H, QI Lu, WANG Ji-qiang, XIONG Tian-ying. A hybrid approach to improve microstructure and mechanical properties of cold spray additively manufactured A380 aluminum composites [J]. Materials Science and Engineering: A, 2020, 772: 138828.

[17] HUTASOIT N, JAVED M A, RASHID R A R, WADE S, PALANISAMY S. Effects of build orientation and heat treatment on microstructure, mechanical and corrosion properties of Al6061 aluminium parts built by cold spray additive manufacturing process [J]. International Journal of Mechanical Sciences, 2021, 204: 106526.

[18] GUO Feng, JIANG Wei, TANG Guang-ze, XIE Zhi-wen, DAI Hong-bin, WANG En-hao, CHEN Yong-jun, LIU Li-jun. Enhancing anti-wear and anti-corrosion performance of cold spraying aluminum coating by high current pulsed electron beam irradiation [J]. Vacuum, 2020, 182: 109772.

[19] WANG Wen, HAN Peng, PENG Pai, ZHANG Ting, LIU Qiang, YUAN Sheng-nan, HUANG Li-ying, YU Hai-liang, QIAO Ke, WANG Kuai-She. Friction stir processing of magnesium alloys: A review [J]. Acta Metallurgica Sinica (English Letters), 2020, 33(1): 43−57.

[20] KHODABAKHSHI F, MARZBANRAD B, SHAH L H, JAHED H, GERLICH A P. Friction-stir processing of a cold sprayed AA7075 coating layer on the AZ31B substrate: structural homogeneity, microstructures and hardness [J]. Surface and Coatings Technology, 2017, 331: 116−128.

[21] HUANG Chun-jie, LI Wen-ya, FENG Yan, XIE Ying-chun, PLANCHE M P, LIAO Han-lin, MONTAVON G. Microstructural evolution and mechanical properties enhancement of a cold-sprayed Cu−Zn alloy coating with friction stir processing [J]. Materials Characterization, 2017, 125: 76−82.

[22] HUANG Chun-jie, LI Wen-ya, ZHANG Zhi-han, FU M, PLANCHE M P, LIAO Han-lin, MONTAVON G. Modification of a cold sprayed SiC_p/Al5056 composite coating by friction stir processing [J]. Surface and Coatings Technology, 2016, 296: 69−75.

[23] HODDER K J, IZADI H, MCDONALD A G, GERLICH A P. Fabrication of aluminum–alumina metal matrix composites via cold gas dynamic spraying at low pressure followed by friction stir processing [J]. Materials Science and Engineering: A, 2012, 556: 114−121.

[24] WANG Wen, HAN Peng, WANG Ying-hui, ZHANG Ting, PENG Pai, QIAO Ke, WANG Zhi, LIU Zhi-hao, WANG Kuai-she. High-performance bulk pure Al prepared through cold spray-friction stir processing composite additive manufacturing [J]. Journal of Materials Research and Technology, 2020, 9(4): 9073−9079.

[25] SHARMA M, SCHREIBER J, EDEN T, CHAMPAGNE V. Stress corrosion cracking resistance of cold-sprayed Al 6061 deposits using a newly developed test fixture [J]. Coatings, 2019, 9(7): 445.

[26] ROKNI M R, WIDENER C A, CHAMPAGNE V K, CRAWFORD G A. Microstructure and mechanical properties of cold sprayed 7075 deposition during non-isothermal annealing [J]. Surface and Coatings Technology, 2015, 276: 305−315.

[27] ROKNI M R, WIDENER C A, NARDI A T, CHAMPAGNE V K. Nano crystalline high energy milled 5083 Al powder deposited using cold spray [J]. Applied Surface Science, 2014, 305: 797−804.

[28] AJDELSZTAJN L, SCHOENUNG J M, JODOIN B, KIM G E. Cold spray deposition of nanocrystalline aluminum alloys [J]. Metallurgical and Materials Transactions A, 2005, 36(3): 657−666.

[29] WALKER M. Microstructure and bonding mechanisms in cold spray coatings [J]. Materials Science and Technology, 2018, 34(17): 2057−2077.

[30] ZOU Y, GOLDBAUM D, SZPUNAR J A, YUE S. Microstructure and nanohardness of cold-sprayed coatings: Electron backscattered diffraction and nanoindentation studies [J]. Scripta Materialia, 2010, 62(6): 395−398.

[31] ROKNI M R, WIDENER C A, CRAWFORD G A. Microstructural evolution of 7075 Al gas atomized powder and high-pressure cold sprayed deposition [J]. Surface and Coatings Technology, 2014, 251: 254−263.

[32] ROKNI M R, WIDENER C A, CHAMPAGNE V R. Microstructural evolution of 6061 aluminum gas-atomized powder and high-pressure cold-sprayed deposition [J]. Journal of Thermal Spray Technology, 2014, 23(3): 514−524.

[33] LIU Zhi-ying, WANG Hong-ze, HACHÉ M, IRISSOU E, ZOU Y. Formation of refined grains below 10 nm in size and nanoscale interlocking in the particle–particle interfacial regions of cold sprayed pure aluminum [J]. Scripta Materialia, 2020, 177: 96−100.

[34] CHEN S F, LI D Y, ZHANG S H, HAN H N, LEE H W, LEE M G. Modelling continuous dynamic recrystallization of aluminum alloys based on the polycrystal plasticity approach [J]. International Journal of Plasticity, 2020, 131: 102710.

[35] ZHANG Yin-yin, SAO-JOAO S, DESCARTES S, KERMOUCHE G, MONTHEILLET F, DESRAYAUD C. Microstructural evolution and mechanical properties of ultrafine-grained pure α-iron and Fe−0.02%C steel processed by high-pressure torsion: Influence of second-phase particles [J]. Materials Science and Engineering: A, 2020, 795: 139915.

[36] WANG Wen, YUAN Sheng-nan, QIAO Ke, WANG Kuai-she, ZHANG Sheng-yi, ZHANG Ting, HAN Peng, WU Bing, YANG Juan. Microstructure and nanomechanical behavior of friction stir welded joint of 7055 aluminum alloy [J]. Journal of Manufacturing Processes, 2021, 61: 311−321.

[37] HUANG K, LOGÉ R E. A review of dynamic recrystallization phenomena in metallic materials [J]. Materials & Design, 2016, 111: 548−574.

[38] SUN N, APELIAN D. Friction stir processing of aluminum cast alloys for high performance applications [J]. JOM, 2011, 63(11): 44−50.

[39] ABDULSTAAR M A, AL-FADHALAH K J, WAGNER L. Microstructural variation through weld thickness and mechanical properties of peened friction stir welded 6061 aluminum alloy joints [J]. Materials Characterization, 2017, 126: 64−73.

[40] ZHAO Yong-hao, ZHU Yun-tian, LAVERNIA E J. Strategies for improving tensile ductility of bulk nanostructured materials [J]. Advanced Engineering Materials, 2010, 12(8): 769−778.
[41] WEI Ying-kang, LUO Xiao-tao, CHU Xin, HUANG Guo-shen, LI Chang-jiu. Solid-state additive manufacturing high performance aluminum alloy 6061 enabled by an in-situ micro-forging assisted cold spray [J]. Materials Science and Engineering: A, 2020, 776: 139024.
[42] ZHONG Xiang-qiang, FENG Jiang, YAO Shun-yun. Temperature field modeling and experimental study on ultrasonic consolidation for Al−Ti foil [J]. Journal of Mechanical Science and Technology, 2019, 33(6): 2833−2840.
[43] WANG Wen, CHEN Shan-yong, QIAO Ke, PENG Pai, HAN Peng, WU Bing, WANG Chen-xi, WANG Jia, WANG Yu-hao, WANG Kuai-she. Microstructure, mechanical properties, and corrosion behavior of Mg−Al−Ca alloy prepared by friction stir processing [J]. Acta Metallurgica Sinica (English Letters), 2022, 35(5): 703−713.
[44] ZHANG Lan, ZHONG Hui-long, LI Sheng-ci, ZHAO Hong-jin, CHEN Ji-qiang, QI Liang. Microstructure, mechanical properties and fatigue crack growth behavior of friction stir welded joint of 6061-T6 aluminum alloy [J]. International Journal of Fatigue, 2020, 135: 105556.
[45] TSAKNOPOULOS K, GRUBBS J, SIOPIS M, NARDI A, COTE D. Microstructure and mechanical property evaluation of aluminum F357 powder for cold spray applications [J]. Journal of Thermal Spray Technology, 2021, 30(3): 643−654.
[46] YANG Xia-wei, LI Wen-ya, YU Si-qi, XU Ya-xin, HU Kai-wei, ZHAO Yao-bang. Electrochemical characterization and microstructure of cold sprayed AA5083/Al_2O_3 composite coatings [J]. Journal of Materials Science and Technology, 2020, 59: 117−128.
[47] CAO Min, LIU Li, YU Zhong-fen, FAN Lei, LI Ying, WANG Fang-hui. Electrochemical corrosion behavior of 2A02 Al alloy under an accelerated simulation marine atmospheric environment [J]. Journal of Materials Science and Technology, 2019, 35(4): 651−659.
[48] REN Jian-ming, MA Jian-bo, ZHANG Jiao, FU Chao-peng, SUN Bao-de. Electrochemical performance of pure Al, Al−Sn, Al−Mg and Al−Mg−Sn anodes for Al−air batteries [J]. Journal of Alloys and Compounds, 2019, 808: 151708.
[49] RAFIEAZAD M, CHATTERJEE A, NASIRI A M. Effects of recycled powder on solidification defects, microstructure, and corrosion properties of DMLS fabricated $AlSi_{10}Mg$ [J]. JOM, 2019, 71(9): 3241−3252.
[50] TAO Yong-shan, XIONG Tian-ying, SUN Chao, KONG Ling-yan, CUI Xin-yu, LI Tie-fan, SONG Guang-ling. Microstructure and corrosion performance of a cold sprayed aluminium coating on AZ91D magnesium alloy [J]. Corrosion Science, 2010, 52(10): 3191−3197.
[51] KUMAR S, RAO A A. Influence of coating defects on the corrosion behavior of cold sprayed refractory metals [J]. Applied Surface Science, 2017, 396(1): 760−773.
[52] SANDER G, TAN J, BALAN P, GHARBI O, FEENSTRA D R, SINGER L, THOMAS S, KELLY R G, SCULLY J R, BIRBILIS N. Corrosion of additively manufactured alloys: A review [J]. Corrosion, 2018, 74(12): 1318−1350.
[53] XIA Da-hai, BEHNAMIAN Y, LUO Ji-li. Factors influencing sulfur induced corrosion on the secondary side in pressurized water reactors (PWRs) [J]. Journal of the Electrochemical Society, 2019, 166(2): 49−64.
[54] ZHOU Bo, LIU Bo, ZHANG Shen-gen, LIN Rui, JIANG Yu, LAN Xue-ying. Microstructure evolution of recycled 7075 aluminum alloy and its mechanical and corrosion properties [J]. Journal of Alloys and Compounds, 2021, 879: 160407.

冷喷摩擦复合增材制造 6061 铝合金的显微组织、力学性能和腐蚀行为

刘志浩[1,2]，韩 鹏[1]，王 文[1]，关肖虎[1]，王 智[1]，方 园[1]，乔 柯[1]，叶东明[1]，蔡 军[1]，谢迎春[2]，王快社[1]

1. 西安建筑科技大学 冶金工程学院 功能材料加工国家地方联合工程研究中心，西安 710055；
2. 广东省科学院 新材料研究所 现代表面工程技术国家工程实验室，
广东省现代表面工程技术重点实验室，广州 510651

摘 要：采用冷喷摩擦复合增材制造(CFAM)技术制备 6061 铝合金块体材料。采用 OM、SEM 和 EBSD 对冷喷涂(CS)和 CFAM 试样的显微组织进行表征，通过显微硬度、拉伸和腐蚀实验研究两者的力学性能和腐蚀行为。结果表明，与 CS 试样相比，CFAM 试样的显微组织更加致密和均匀，晶粒细小等轴，平均晶粒尺寸为 3.1 μm，显微硬度、极限抗拉强度和伸长率分别提高了 22%、171%和 683%。CFAM 试样的腐蚀电流密度比 CS 试样低 95.1%~97.8%，腐蚀机理由 CS 试样的点腐蚀转变为晶间腐蚀。

关键词：冷喷摩擦复合增材制造；6061 铝合金；显微组织；力学性能；腐蚀机理

(Edited by Wei-ping CHEN)